Paper III

Christina A. Pedersen, Richard Hall, Sebastian Gerland, Agnar H. Sivertsen, T. Svenøe and Christian Haas, "Combined Airborne Profiling over Fram Strait Sea Ice: Fractional Sea-Ice Types, Albedo and Thickness Measurements", submitted to *Cold Region Science and Technology*, 2007.

Combined Airborne Profiling over Fram Strait Sea Ice: Fractional Sea-Ice Types, Albedo and Thickness Measurements

C. A. Pedersen [a,*] R. Hall [a,1] S. Gerland [a] A. H. Sivertsen [b]
T. Svenøe [a] C. Haas [c,2]

[a]*Norwegian Polar Institute, Tromsø, Norway*
[b]*Fiskeriforskning, Tromsø, Norway*
[c]*Alfred Wegner Institute for Polar and Marine Research, Postdam, Germany*

Abstract

This paper describes the data collected during an expedition from the marginal ice zone into the multi year sea ice in the Fram Strait in May-June 2005 to measure the variance in sea-ice types, albedo and thickness, and the techniques used to analyze the data. A combination of methods was used to extract more information from each data set compared to what originally and traditionally are obtained. The principal information from the three methods applied give the sea-ice types from digital photography, the spectral and broadband reflectance factor from a spectrometer and the thickness profile from a electromagnetic-"bird", with emphasize on using, adapting and combining the different techniques. The digital images was standardized, textural features extracted and a trained neural network was used for classification, while the optical measurements were normalized and standardized to minimize effects from the set up and atmospheric conditions. The fractional sea-ice types proved to have large spatial variability, with average fractions for snow covered sea-ice of 81.0%, thick bare ice 4.0%, thin ice 5.3% and open water 9.6%, ergo an average ice concentration of 90.3%. The average broadband reflectance factor was 0.73, while the mean sea-ice thickness (including snow) was 2.1 m. Relative high correlations were found between the measured albedo and sea-ice concentration (0.69), however, the correlation would probably be higher if it were not for the possible tilt of the helicopter and offsets in the co-location procedure. The paper also addresses the lessons learned for future fusion of data from large field campaigns.

Key words: sea ice, airborne measurements, albedo, classification

1 Introduction

Sea ice is a complex heterogeneous cover which plays an important role in the Earth's climate system. To obtain a better understanding of the distribution of sea ice, *in situ* data are collected during field campaigns. However, scientific-based operations in the Polar Regions are limited, mainly due to the cost of such operations, ship availability and competition from other scientific programmes for ship-time. Therefore, when opportunities to collect multiple data sets arise, it is important to co-ordinate all activities to ensure that not only are as many parameters as possible covered efficiently, but also that the data can be easily combined and compared for further analysis.

This paper describes the data collected during an expedition from the marginal ice zone into the multi-year sea ice in the Fram Strait in May-June 2005 to measure the variance in sea-ice types, albedo and thickness, and the techniques used to analyze the data. A combination of methods was used to extract more information from each data set compared to what originally and traditionally are obtained. The classification of sea-ice types only involved surfaces identified during winter and spring conditions (that is, snow covered sea ice, bare ice, thin ice and open water). *E.g.* melt ponds were not included since the onset of melt had not started at the time of the measurements. However, the provided techniques are quite general so only minor changes are required to include *e.g.* melt ponds or other necessary sea ice types. A main question addressed is how albedo varies in relation to the type of sea ice. While there is a simple relationship where thick ice has a high albedo and thin ice has a low albedo, this only applies to thin ice covers up to 30 cm thick under cold winter conditions (Laine, 2004). However, under summer conditions in the Arctic Ocean, the correlation between albedo and sea-ice concentration (extent) extracted from remote sensing data is found to be only 0.34 (0.40), with large variability between individual spatially areas (Laine, 2004). For the Northern Hemisphere as one the numbers are 0.56 (0.50).

Previous studies on classifying sea-ice types from helicopter images has mostly concerned identifying melt ponds. As part of the Surface Heat Budget of the Arctic Ocean (SHEBA) field experiment aerial photography and video camera flights were completed between spring and autumn in 1998 (Perovich et al., 2002; Tschudi et al., 2001). Perovich et al. (2002) calculated fractions of ice, new ice, ponds and leads using imaging processing software and manually selected thresholds based on histograms, while Tschudi et al. (2001) identified melt pond and open water fractions from video images using spectral

---
* Corresponding author.
  Email address: christina.pedersen@npolar.no (C. A. Pedersen).
[1] Present address: Kongsberg Satellite Services, Tromsø, Norway
[2] Present address: University of Alberta, Edmonton, Alberta, Canada

information in the three RGB bands of the converted images. Other previous studies include Derksen et al. (1997) employing low level aerial infrared photographs for identifying melt pond fractions, and Fetterer and Untersteiner (1998) utilizing maximum likelihood algorithms to select a threshold intensity to separate pond distribution from ice distribution. More advanced classification tools for detecting sea-ice types were used in studies analyzing Synthetic Aperture Radar (SAR) images. Although the SAR scenes have a much coarser spatial resolution than the aerial photography presented in this paper, some of the techniques applied can be adapted to the photographs. Bogdanov et al. (2005) used a neural network and linear discriminate analysis together with data fusion to automatic classifying SAR sea-ice images. Substantial improvements were gained by fusion of several data types. Texture statistics from grey level co-occurence matrix was used in Barber and Le Drew (1991). Also a few approaches applied to optical remote sensing data exist. A data fusion algorithm involved iterative segmentation procedure on SAR images and extraction of spectral characteristics from AVHRR images, resulted in distinguishing between six sea-ice types (Lythe et al., 1999). Markus et al. (2002) used a threshold based algorithm on individual Landsat bands to distinguish between white ice, bare/wet ice, melt ponds and open water.

This paper presents an interfusion of methods for characterizing individual sea-ice types by discriminating between snow covered sea-ice, thick bare ice, thin ice and open water based on the measurements from the airborne sea ice profile. Digital images, optical reflectance measurements and electromagnetic thickness measurements were combined to obtain a detailed description of the sea-ice physical and optical properties. Sec. 2 gives an overview of the experimental set-up and measurements conducted during the expedition in the Fram Strait spring 2005. We describe in detail the methods used to analyze the images, including standardization and cross-correlation (Sec. 3.1.1), feature extraction (Sec. 3.1.2) and classification (Sec. 3.1.3). The optical measurements are discussed in Sec. 3.2, and co-location and fusion (including spectral unmixing) of the three datasets in Sec. 3.3. Results and discussions on the individual datasets are given for sea-ice types in Sec. 4.1, reflectance measurements in Sec. 4.2, sea-ice thickness in Sec. 4.3, and data fusion in Sec. 4.4. Conclusions and outlook with lessons learned for future fusion of data collection from large field campaigns are given in Sec. 5.

2   Experiment setup

The Fram Strait represents the main passage for sea ice and water that leaves the central Arctic Ocean, being important for the freshwater balance in the ocean and for ocean circulation and convection (Kwok et al., 2004; Vinje, 2001). In May-June 2005, the Norwegian Polar Institute led a field campaign

3

in the Fram Strait (Fig. 1), where three sets of airborne measurements were collected by helicopter (Tab. 1). Since the optical measurements require a clear field of view underneath the helicopter two separate flights were carried out. The first flight included digital photography and optical measurements, while the second was for the electromagnetic (EM) measurements. For the optical flight, the digital camera and the 8° for-optics of the spectrometer were mounted on an aluminum plate and fastened to the floor of the helicopter looking down through a Lexan-glass window (Fig. 2).
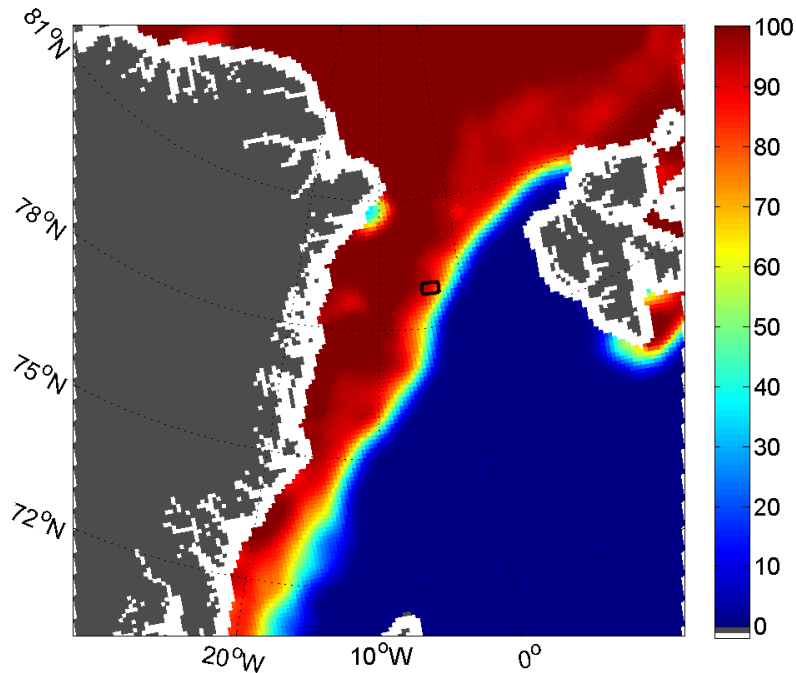

Fig. 1. Sea-ice concentration (in percent) for Fram Strait 3rd June 2005 after met.no, with Svalbard to the right and Greenland to the left (grey is land area and white is no data). The rectangle mark the investigated area 78.00°-79.05° N and 2.8°-4.8° W.

Method	Instrument	Sampling frequency
Fractional sea-ice types	Canon EOS 350D digital camera	5 s
Reflectance	ADS FieldSpec Pro spectrometer	2 s
Ice thickness	Ferra Dynamics electromagnetic "bird"	0.1 s

Table 1
Airborne measurements

The position, speed and altitude of the helicopter were logged with a Global Positioning System (GPS) receiver, and the altitude and speed of the helicopter were restricted so as to receive over-lapping images. A typical optical
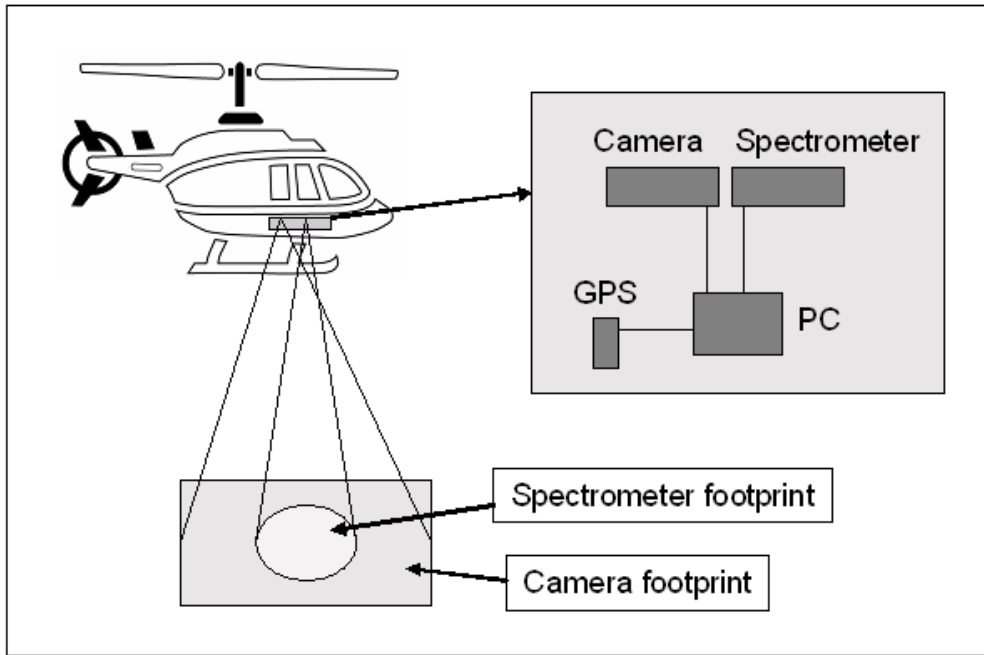
4

Fig. 2. Set up for the optical flight with digital camera and spectrometer for-optics mounted on the floor of the helicopter. The cameras and spectrometers field-of-view are shown relatively to each other.

flight had an image footprint of 200 m in flight direction and 150 m across flight direction, and 50-75 m overlap between successive images. In reality, each pixel in the image footprint are rectangular due to the speed of the helicopter and the exposure time of the camera. A typical foot-print for the spectrometer was for simplicity assumed to be a circle with a diameter of 15-25 m. But similar as for the pixels, the footprint is like to an elliptic due to the helicopter movement during the time taken to conduct a measurement. The reflectance measurements and digital images was co-located post-flight based on GPS time and position. The EM measurements, collected on a separate flight, could not be directly compared to the other measurements, due to a slightly different track and a fast drifting ice cover.

The electromagnetic data for deriving ice thickness was processed following standard routines as described in Haas et al. (1997, 2006), giving the distance between snow surface and ice underside (ice plus snow thickness equaling the total thickness, hereafter described with "ice thickness"). The distance between individual measurement points on the ice is about 3 to 4 m (sampling frequency 10 Hz), and the absolute accuracy of the method is better than 90% Haas et al. (1997).

The spectral albedo is the ratio of reflected to incident irradiance (solar light integrated over the hemisphere), while spectral reflectance is the ratio of reflected to incident radiance (solar light over a restricted field-of-view). The

measurements we collected, spectral reflectance factor (SRF), is the ratio of reflected radiance to incident radiation reflected from a perfect, white, diffuse surface (Spectralon) (Nicodemus et al., 1977). The for-optics of the spectrometer was mounted behind a Lexan window in the helicopter. After the campaign we realized that the curvature of the Lexan window was acting as a collecting lens in the visible, by directing the light towards the for-optic. The Lexan window was also found to have absorption bands at 350-380 nm, at about 1700 nm and above 2200 nm. Also the reflectance spectra showed to have an unexpected peak at UV wavelengths in particular. Probably the Lexan window disturbed the measurements, but the net effect is difficult to assess.

2.1   Description of sea-ice types

The distinction and classification between sea-ice types is not a straight-forward task. While the WMO Sea-Ice Nomenclature (Secretary of World Meteorological Organization, 1970) is the accepted reference, it does not easily allow sufficiently for slight variations in ice cover which can be required in detailed scientific studies. As a result, individual scientific studies developed sea-ice classification schemes based on the WMO, but modified to account for the many variations observed during field campaigns (Armstrong et al., 1966; Steffen, 1986). However, for the purpose in this paper, all these classification schemes are too detailed. Our measurements were collected in spring, before the onset of melt, and four broad and quite general sea-ice types (including snow cover) as given in Table 2, were identified. The classification of the four types were based on visual observations of surface characteristics (Fig. 3) during the cruise. Snow covered- and bare sea ice were separated mainly based on color, since snow has a white appearance compared to the blue-green bare ice. Thin ice covers the broadest range of types with a wide range in spectral reflectivity. It should be thought of as an intermediate type between thick blue-green ice and open water. Thin ice is separated from the other classes with its grayish color (it also include the masses consisting of small ice-floes partly within the new ice). The open water is easily separated from the others with its dark appearance due to the relative constant very low 0.07 value over the visual part of the spectrum (Brandt et al., 2005). The open water class also includes dark nilas. The four classes correspond well with other ice types chosen for classification (Massom and Comiso, 1994), as the unambiguous distinction of more ice types may be difficult. However, after the onset of melt the picture is quite different with large areas of melting, wet snow and melt ponds on the ice. The techniques described in the next sections are general, so inclusion of more sea-ice types is relatively strait forward.

Class index	Description of sea-ice types
I	Snow covered sea ice
II	Thick bare sea ice
III	Thin ice (grey ice and light nilas)
IV	Open water

Table 2
Observed sea-ice types from the marginal ice zone into the multi year sea ice in spring 2005 in the Fram Strait.
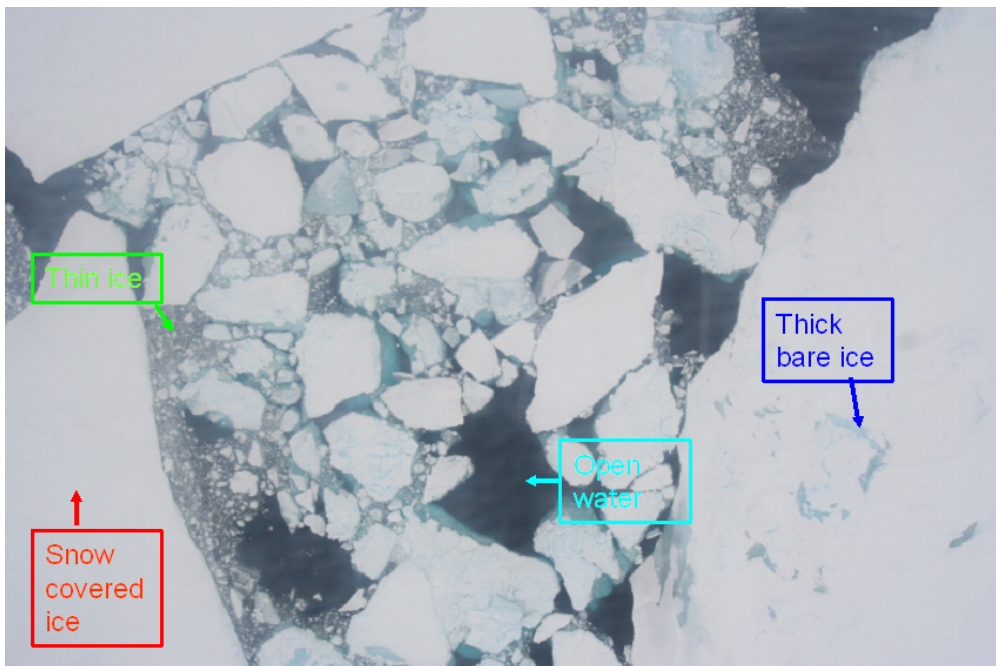

Fig. 3. Sea-ice image example where each of the four sea-ice types are represented. The colors correspond to the spectra in Fig. 5.

3 Data analysis

3.1 Digital photography

The images size were originally about 2Mb with an average pixel size equivalent to 0.05 m for a typical helicopter altitude. To reduce the processing time the images were down-sampled by averaging over every 10th pixel, giving a down-sampled image of 230x345 pixels and a resolution of approximately 0.50 m.

3.1.1 Image standardization

The exposure time, aperture opening and white balance parameters of the camera were set to automatic, and therefore the color intensity of the images was scaled according to the amount of light and dark pixels in the image. For example, the snow in an image consisting of only snow (bright pixels) seemed darker than the snow in an image consisting of both snow and open water (bright and dark pixels), as also experienced by others (Derksen et al., 1997). The brightness was not constant across the images, and particularly for snow we experience darker intensities along the edges due to vignitation, however, it did not cause a major problem and is not corrected for. The white balance in the images required corrections for by standardizing the images according to the following iterative procedure (Fig. 4): The first image with good contrast was selected and scaled to an appropriate range. The sub-image of 100 pixels in the flight direction from two succeeding and overlapping images (last 100 pixels from the first image and first 100 pixels from the second image) were normalized and cross-correlated. The maximum in the cross-correlation matrix gave the position where the two images were aligned or had best match. The second sub-image were normalized so that the two overlapping sub-images had the same mean and standard deviation. Due to the angle and tilt and variable speed of the helicopter, the images did not completely overlap in the flight direction, and for some images manual adjustments were requisite.

3.1.2 Feature selection

Every pixel in an image was classified separately based on 14 features for texture characterization according to Theodoridis and Koutroumbas (1999) (Tab. 3). Feature 5-11 were calculated inside a 7×7 sliding window of the grey-leveled indexed image, and provide information related to the grey level distribution of the image, but do not give information about the relative positions of the various gray levels within the image. Feature 12-14 is based on the second-order histogram, consider pixels in pairs and investigate the relative distance and orientation between them. Maximum discrimination between SAR sea-ice types was obtained when considering gray level co-occurrence matrix with parallel pixels with an interpixel distance of one (Barber and Le Drew, 1991), and that approach was followed for feature 12-14.

The best features for separating between snow covered ice, thick bare ice, thin ice and open water were selected according to Fisher Discriminant Analysis (Johnson and Wichern, 2002). Fisher Discriminant Analysis is a transformation of the multi-variate observations from the feature space into the Fisher space, where it selects the linear combination of features to achieve maximum separation between the classes. The Fisher discriminant is calculated based on feature vectors with known classification label, which require a training
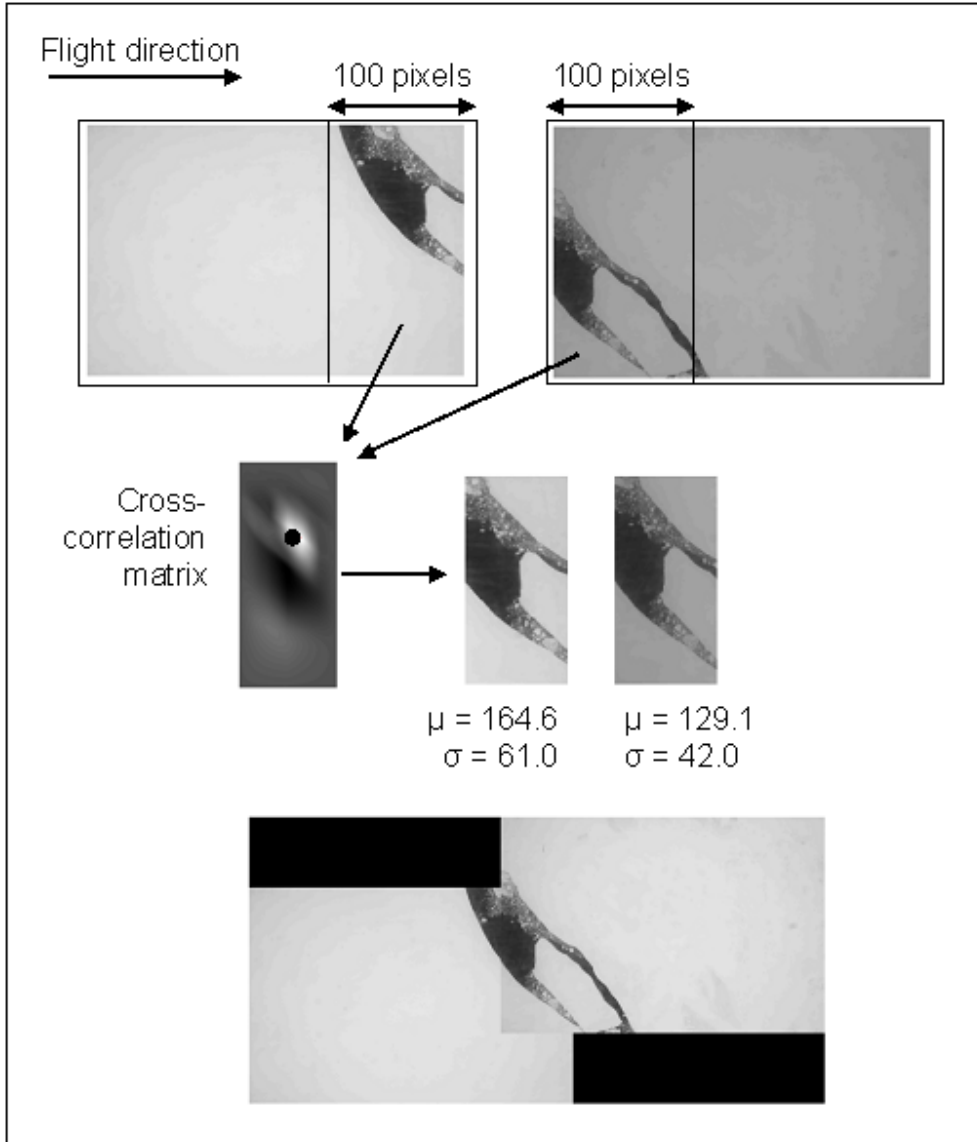
Fig. 4. The standardizing procedure for getting a homogeneous time series of the airborne images. The upper panels show two succeeding and overlapping images with different brightness and contrast. The two sub-images (of 100 pixels width, marked with a frame) were cross-correlated, giving the matrix in the middle left. The black dot marks the maximum in the cross-correlation matrix, giving the best alignment between the sub-images (shown in the middle-right). The second sub-image was scaled to have the same mean (μ) and standard deviation (σ) as the first. The bottom image shows the two standardized and overlapping images after the standardization procedure.

and test set of data where the class is known. The training set is used for constructing the classifier, while the test data is used for testing the performance of the classifier. The test and training data sets were created by manual classification of the four sea-ice types. Each combination of features (choose k out of 14 features, where $k = 1, ..., 14$, is 16 384) were tested by calculating

	Feature
1	Red intensity
2	Green intensity
3	Blue intensity
4	Grey-level intensity
5	Mean intensity
6	Variance
7	Skewness
8	Kurtosis
9	Entropy
10	Energy
11	Coefficient of variance
12	GLCM contrast
13	GLCM energy
14	GLCM homogeneity

Table 3
Textural features for sea-ice classification. Feature 5-11 is based on first order statistics, while feature 12-14 is from second-order statistics and the grey-level-co-occurrence matrix (GLCM)

the Fisher discriminant, applying the Fisher classification rule (Johnson and Wichern, 2002) and evaluate the total average classification error based on feature vectors with known classification belonging. The set of features giving the smallest classification error was chosen for further investigations.

3.1.3 Classification

For classification a feed-forward back propagation neural network (Haykin, 1999) with 3 layers was used. The first layer has a size (number of neurons) equal to the number of features, the hidden layer has two times the number of features neurons, and the output layer has one neuron (separating the four classes on the interval [0,1]). All neurons have the log-sigmoid as the activation function. The neural network is trained by presenting feature vectors with known classification label to the network, and the network updates its weight to minimizing the sum of squared error and achieve the expected output in an adaptive manner.

Classification based on texture features (calculated over a sliding window) often experience problems on the edge between classes. *E.g.*, an image con-

sisting of a sharp edge between snow covered ice and open water will in the classified image often have a small transition zone where intermediate classes (bare ice or thin ice) are detected. Since the median filter is particular effective in reducing noise while at the same time preserve edge sharpness (Gonzalez and Woods, 1992), the classified images were median filtered (with a filter size equal to the window size used for extracting the texture features). This approach was also used by others (Tschudi et al., 2001; Derksen et al., 1997).

3.2   Optical measurements

The reflected radiance from the Spectralon was collected before and after the flight, only the reflected surface radiance were collected during the flight. The reflected surface radiance is affected by the amount of clouds, and change as clouds drift, so variable light conditions results in error in the SRF (both in terms of spectral signature and absolute value). To reduce the effect of changing light conditions and overcome some of the shortcomings with the set-up, the SRF measurements were normalized with the ratio of the reflectance over a large, homogeneous, snow-covered surface both from inside the helicopter when flying and from the ground afterwards, as also done by Allison et al. (1993) on their optical airborne measurements. As the irradiance changed, slightly, but notably, during the flight, the SRF measurements were also scaled to minimize that effect. Some aspects regarding the variable foot-prints of the helicopter and ground measurements and the time difference and changing light conditions between the helicopter and ground measurements may be used to questions this normalization, but all together, we think it is the most reasonable data standardization we can do.

3.3   Data fusion

The reflectance measurements and images were co-located based on time and position. For each reflectance spectra the foot-print in the image was identified and the fractions of sea-ice types within that footprint calculated (Fig. 5). As the co-location was based on time (resolution 1 s) and the helicopter had an typical speed of 25-30 ms$^-1$, some error in the co-location procedure must be assumed. Angle and tilt of the helicopter change the direction of the spectrometer footprint, and tilt errors is subject to change the albedo (more under clear sky, and less for overcast Allison et al. (1993)). Visual inspection of examples containing measurements over changing surfaces confirmed that these errors principally were small, and no attempt was made towards correcting for this.
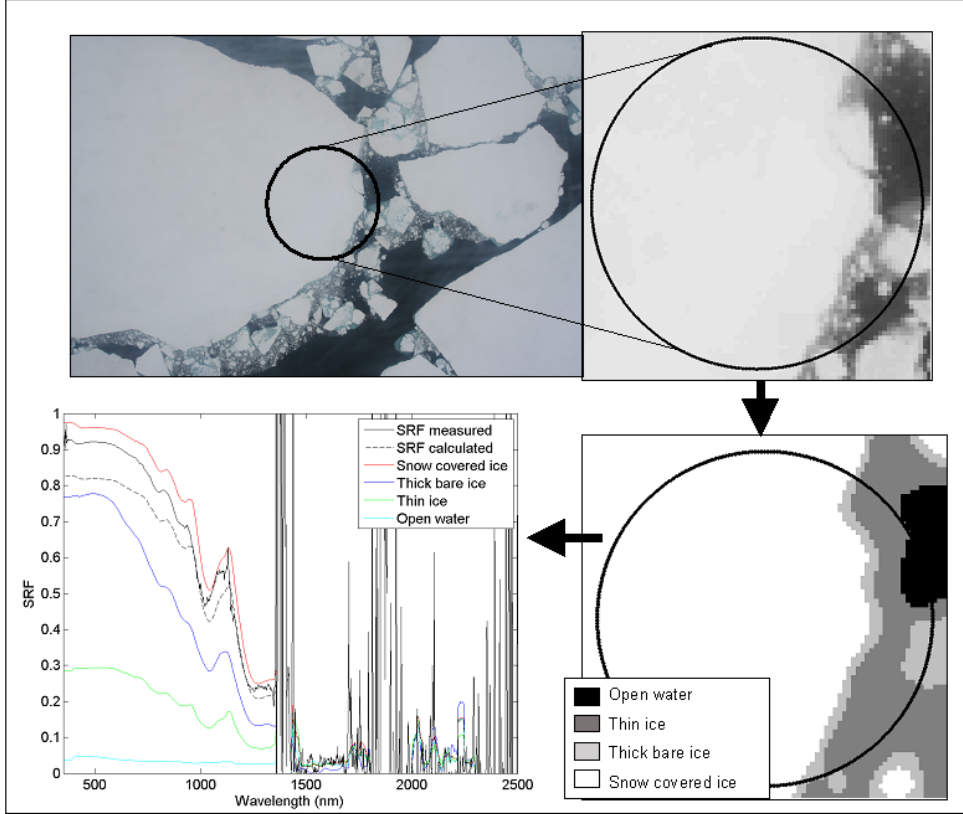
Fig. 5. An example of the co-location procedure of the data, with the original RGB image (upper panel, left), and the footprint of the spectrometer co-located within the grey-leveled, down-sampled image (upper panel, right). The classified subset of the image (bottom panel, right) gives a fraction of 75.8%, 5.5%, 16.0% and 2.7% for snow covered ice, thick bare ice, thin ice and open water, respectively, with the corresponding characteristic curves (endmembers) for the four sea-ice types (in color) together with the measured and calculated spectral reflectance factor (SRF) (bottom panel, right).

3.3.1 Spectral unmixing

Spectral unmixing is an unsupervised classification technique based on the spectral reflectances, by modeling the measured reflectance spectra as a linear combination of characteristic reference spectra (so-called endmembers). If the endmembers are known, the product of the spectral unmixing gives the fraction of each sea-ice type within the spectrometer foot-print by solving (Vikhamar, 2003)

$$\mathbf{f} \cdot \alpha_{\mathbf{ch}}(\lambda) = \mathbf{r}(\lambda) \tag{1}$$

in a least square manner. $\mathbf{f}$ is the $(m \times 4)$ matrix of fractions for the four sea-ice types for m images, $\mathbf{r}(\lambda)$ is the $(m \times n)$ matrix of measured reflectance spectra, and $\alpha_{\mathbf{ch}}(\lambda)$ is the $(4 \times n)$ characteristic albedo curves for each sea-ice type. n

12

is the number of wavelength bands. The endmembers were identified directly from the classified images (the fraction of sea-ice types within the spectrometer footprint in the image) and the spectral reflectance measurements by using inverse spectral unmixing. This was done in a partly iterative manner, by first assuming standard characteristic albedo curves from previous measurements, as suggested by Tschudi et al. (2001). Based on the classified image fractions and the endmembers, an additional measure of SRF could be calculated by weighting the characteristic spectra with the fractions in the spectrometer foot-print, as done in Perovich et al. (2002).

4   Results and discussion

This section presents the measurements collected from the marginal ice zone into the multi year sea ice in the Fram Strait on 3rd June 2005. This day was chosen because the sky was overcast with reasonable stable light as required by the optical measurements. All together 592 images, 1 487 spectra and 26 488 thickness signals were standardized and classified (Sec. 3). The airborne measurements were collected from a transect going east-west-north-east for optics and photography and east-west-east for EM-measurements (Fig. 6). The two east-west transects, seen relative to the ice surface, become more distant to the east as the ice in the western Fram Strait drifts relatively fast in S-SW direction. From 3°W to 4° 36' W the EM bird flight-line coincides more or less with the first east-west transect of the optical flight, so these sections are taken out for comparing sea-ice thicknesses with findings and characteristics from the optics and photography. Taking the relatively fast ice drift in the western Fram Strait into account, we expect that this comparison is only possible when assessing the general ice regime characteristics, and not individual floe with high spatial resolution.

The next paragraphs describe the principal information obtained from each instrument, as well as information obtained from spectral unmixing/inverse spectral unmixing and data fusion. The fractional sea-ice types (Sec. 4.1) are the principal information from neural network classification of the digital images, but was also calculated from spectral unmixing of the optical data and thresholding of the thickness data as proxies for comparisons. The spectral and broadband reflectance factors (Sec. 4.2) are the principal information from the optical measurements, however, optical properties were also calculated from inverse spectral unmixing of the classified images. The sea-ice thickness (Sec. 4.3) can only be calculated from the EM-measurements. In Sec. 4.4 the relationship and correlation between fractional sea-ice types, optical properties and sea-ice thickness are investigated.
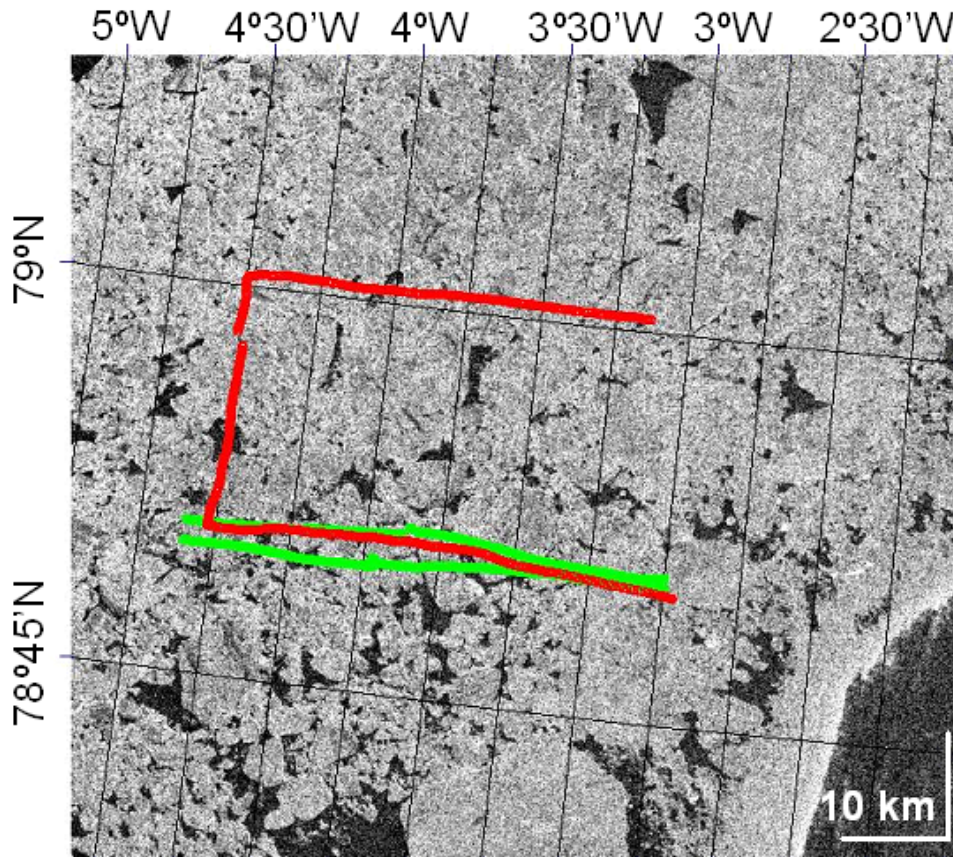
Fig. 6. Flight track for the two helicopter flights on 3rd June 2005 in the Fram Strait. The red track is for the optical and photography measurements, while the green is for the electromagnetic measurements (only the measurements between 3-4.6°W are shown and was used, however the track expands to from 2°-10°W). Keep in mind the time difference: the SAR image is from 07.31 GMT, the optical flight was compiled between 07:27-08:19 GMT, and the electromagnetic flight between 11:08-12:32 GMT. The sea ice in the Fram Strait drifts relative fast in S-SW direction, so even if the two track coincide in position they did not cover the same area relative to the ice.

4.1 Sea-ice types

The test and training data sets (Sec. 3.1.3) were created by manually classifying 120 000 pixels within 23 images to each of the four sea-ice classes. The best set of features were selected according to Fisher Discriminant Analysis (Sec. 3.1.2) by performing 50 Monte Carlo simulations where the test and training set were chosen randomly within the set of classified pixels for each simulation. The best features for separating between the sea-ice classes were found to be the three RGB intensities, the co-efficient of variance (standard deviation divided by the mean), the entropy (measure of histogram uniformity) and the GLCM homogeneity. The mean plus/minus one standard deviation

for the RGB intensities was found to separate the four classes completely, only with slight overlap between thin ice and open water. The co-efficient of variance was high for thin ice, and the mean plus/minus one standard deviation separates it from the other classes, while the mean of the entropy plus/minus one standard deviation separates thick bare ice from thin ice. No such simple relationship was found for the GLCM homogeneity.

The neural network proved to be extremely efficient for discriminating between the four sea-ice types, with only 1.06% classification error on the test set. The confusion matrix give the number of times a feature vector belonging to class i (row) is classified to class j (column), where i, j are the four classes (Table 4). The correct classified pixels are along the diagonal from upper left to lower right. The test resulted in 98-100% correct classification for the different classes, which is more than sufficient for routine use. Open water can easily be distinguished from the other types, with only 0.2% confusion with thin ice. Thick bare ice is most often confused with snow covered ice (1.0%). Large scale structures (such as large areas of open water or snow covered sea ice) are generally easily identified both from the original and the classified image (Fig. 5). At smaller scales, the classification is less accurate due to down-scaling and smoothing when calculating the texture features. Errors on the edges between classes are typical (the median filter (Sec. 3.1.3) does not completely remove this) and the consequences are that the intermediate sea-ice types (thick bare ice and thin ice) are over-estimated. The test set results underestimate the classification error since the pixels in the test set was chosen within larger, relative homogeneous areas of the individual sea-ice types, and fewer pixels were on the edge between classes. For images outside the test set, larger classification error is expected, particularly for thick bare ice and thin ice covering relative small areas. Remember the textural features are averages over a 3.5 m x 3.5 m window, and features smaller than 3.5 m x 3.5 m (*e.g.* wind shaped formations in snow, small ice floes and blocks, pancake ice *etc.*) will be removed by smoothing and not identified.

	Snow covered ice	Thick bare ice	Thin Ice	Open water
Snow covered ice	**98.4**	1.3	0.2	0.1
Thick bare ice	1.0	**98.3**	0.5	0.2
Thin Ice	0	0.6	**99.2**	0.2
Open water	0	0	0.2	**99.8**

Table 4
The confusion matrix for neural network classification on the test set, when the best feature combination (the three RGB intensities, co-efficient of variance, entropy and GLCM homogeneity) was used. The confusion matrix gives the number of times a feature vector belonging to class i (along the rows) is classified to class j (along the columns). The correct classified pixels are in bold along the diagonal.

15

The fractional area of snow covered ice, thick bare ice, thin ice and open water as a function of longitude bands show considerable spatial variability, with snow covered ice fractions varying from 0 to 100%, but with an average high ice concentrations over the entire profile (Figs. 7a and 6). The two ice classes without snow cover represent only a small portion compared to snow covered ice and open water. In the western part there are more areas of open water. Overall, the average ice concentration (total of snow covered, thick and thin ice) was 90.4%, with average fractions for snow covered sea-ice of 81.0%, thick bare ice 4.0%, thin ice 5.3% and open water 9.6%. For comparison, the average sea-ice concentration compiled from Norwegian Meteorological Institute from remote sensors Andersen et al. (2005) were 82.8% (with median 83.7% and range 64.0-93.9%) for the twelve 10 km resolution pixels inside the rectangular area of Fig. 1.
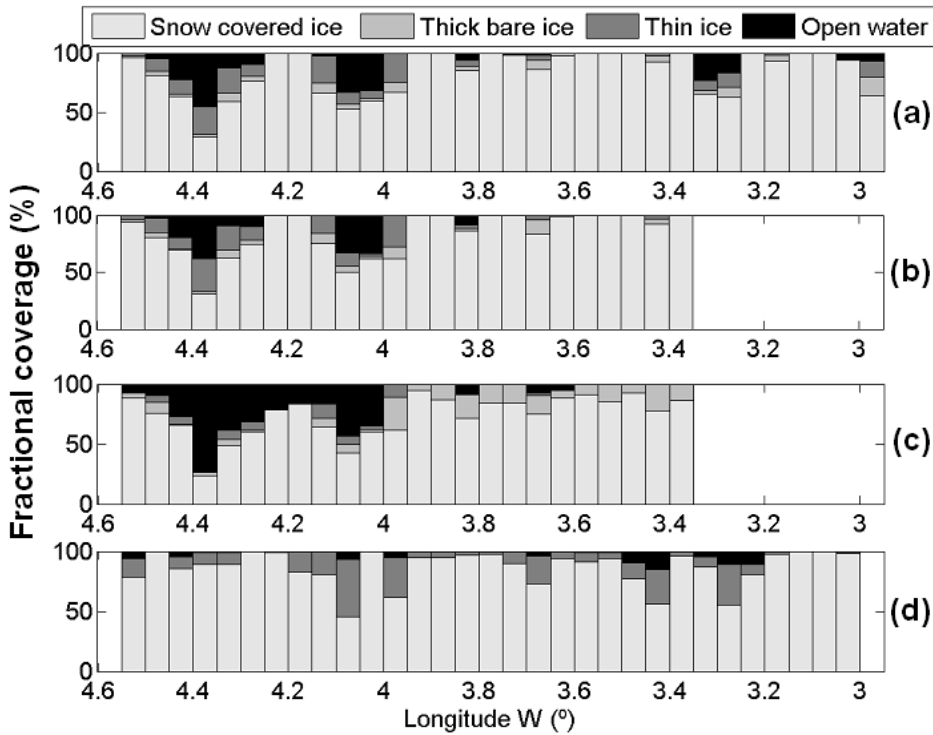

Fig. 7. Fractional coverage of open water, thin ice, bare thick ice and snow covered ice as a function of longitude bands of 0.05°. (a) is neural network classification from photography, (b) is neural network classification from photography within the footprint of the spectrometer (only a subset of the image is used), (c) is spectral unmixing from optical measurements, (d) is classification based on EM thickness measurements. The bottom panel only has three classes (open water (black), thin ice (grey) and thick, snow covered ice (light grey)).

The neural network classification is the principal information from the digital images and proved to have very small classification error on the test set so it is taken to represents the true sea-ice classes, while the spectral unmixing of

optical measurements and thresholding of the ice thickness measurements are taken to be proxies. The spectral unmixing technique overestimates the open water fraction to the west and the thick bare ice to the east (Fig. 7). It has difficulties in detecting thin ice, which is clearly seen in Fig. 7, where the thin ice in the west is detected as open water. The correlation coefficient between the fractions from the neural network and spectral unmixing is highest for snow covered ice (0.90) and open water (0.81), whereas for the two intermediate sea-ice classes the correlation coefficient is substantially smaller, only 0.51 for thick bare ice and 0.58 for thin ice. Limitations in the co-location and tilt of the helicopter is probably responsible for most of the deviations, particularly for the two intermediate types covering smaller spatially areas thereby being more sensitive to small off-sets. A scatter-plot of neural network fractions (f_{NN}) against spectral unmixing fractions (f_{SU}) (Fig. 8), show a cluster along $f_{NN} = 1$ (Fig. 8a), meaning that the spectral unmixing is underestimating the snow covered ice. For thick bare ice and open water (Figs. 8 b and d, respectively) the trend is opposite, with clusters along $f_{NN} = 0$, implying the spectral unmixing overestimates those fractions. For thin ice (Fig. 8 c) the congestion is along $f_{SU} = 0$, meaning that the spectral unmixing has problems in detecting thin ice. The overall root mean square error for using spectral unmixing to estimate the fractions are 0.034, 0.027, 0.021 and 0.028 for snow covered ice, thick bare ice, thin ice and open water, respectively.

The EM thickness measurements were classified by separating between open water (thickness below 0.05 m), thin ice (thickness between 0.05-0.3 m) and thick snow-covered ice (thickness above 0.3 m). It is not possible to partition the snow and the ice from the EM measurements, since the snow thickness is always included in the total thickness. The fractions from the EM measurements show different characteristic, with no trend, and mostly thick (snow covered) sea-ice at all longitudes (Fig. 7 d). These fractions can not be compared directly with the others, as the two flight lines did not immediate coincide in time. If adding up the snow covered and thick ice fractions from neural network and comparing it with the thick ice fraction from the EM measurements, the correlation coefficient is only 0.25, with corresponding correlation coefficient between the thin ice- and open water fractions are 0.34 and 0.08, respectively.

4.2   Reflectance

Only the first east-west transect of the optical flight was used, as the light conditions changed too much over time as to include all measurements. The broadband reflectance factor (BRF), calculated from the SRF measurements by weighing the spectral reflectance with an appropriate solar irradiance specter for cloudy conditions (Grenfell and Perovich, 2004) (hereinafter called mea-
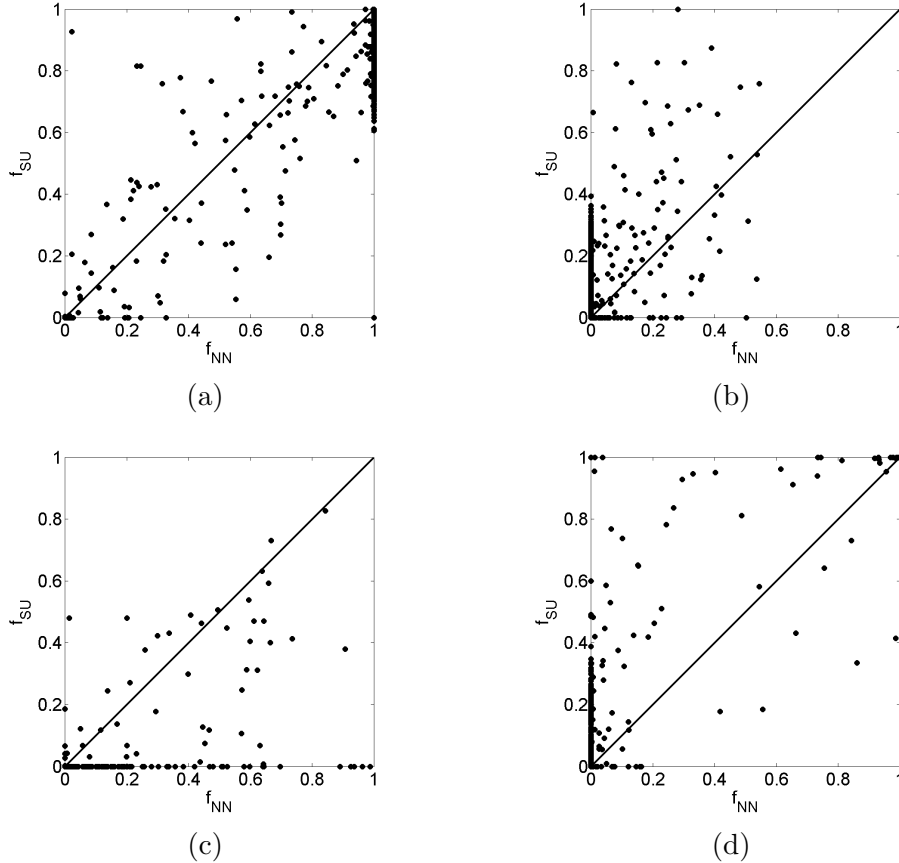
Fig. 8. Scatter plot between sea-ice fractions as calculated from neural network (f_{NN}) and spectral unmixing (f_{SU}). The 1:1 line indicates linear correlation. (a) is for snow covered ice ($\rho = 0.90$), (b) thick bare ice ($\rho = 0.51$), (c) thin ice ($\rho = 0.58$) and (d) open water ($\rho = 0.91$), where ρ is the correlation coefficient.

sured BRF) show relative high mean BRF values over the entire transect, however higher in the east than in the west (Fig. 9). As the broadband albedo is higher for cloudy than clear sky Brandt et al. (2005), this indicate more clouds with time. The average BRF was 0.73 with standard deviation of 0.33. The BRF was also calculated from inverse spectral unmixing (hereinafter called calculated BRF), and corresponds well with the measured BRF (Fig. 9). However, the calculated BRF does not increase towards the east since it has its upper threshold value at 0.8711 corresponding to a completely snow covered surface. The scatter plot of measured versus calculated BRF (Fig. 10) show that the measurements coincide around the 1:1 line, with correlation coefficient of 0.94. Measured BRF are higher than calculated BRF for high values (the measured BRF frequently exceeds one), with a weak tendency of the opposite for small BRF values. If the measured BRF is taken to represent ground truth reflectance factor, the overall root mean square error for calculated BRF is 0.048.

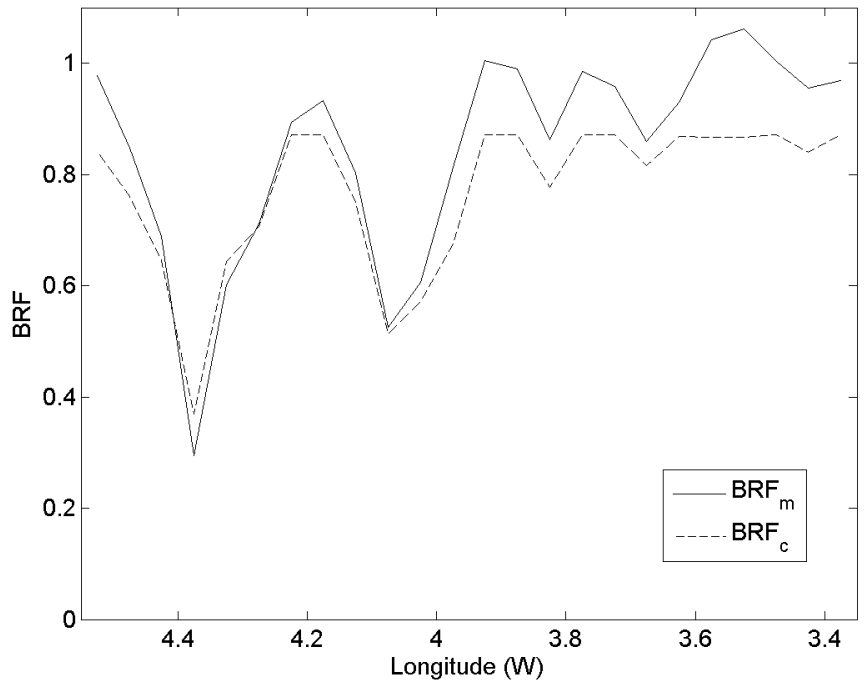The endmembers for the four sea-ice types were calculated from inverse spec-

18

Fig. 9. Measured (BRF$_\mathrm{m}$) and calculated (BRF$_\mathrm{c}$) broadband reflectance factor as a function of longitude bands of 0.05°.
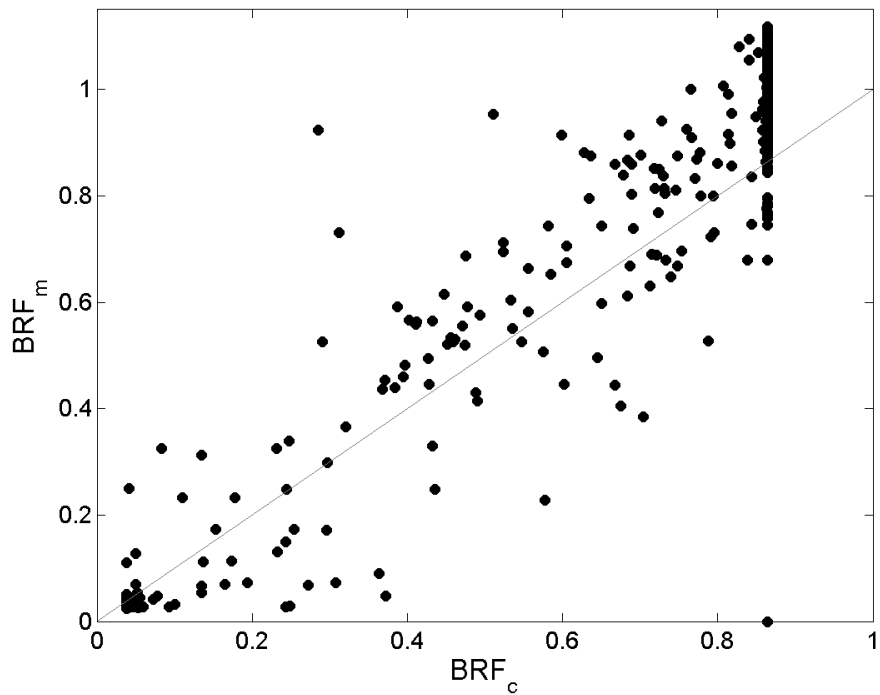

Fig. 10. Scatter plot of measured broadband reflectance factor (BRF$_\mathrm{m}$) against calculated broadband reflectance factor (BRF$_\mathrm{c}$). The correlation coefficient is 0.94.

19

tral unmixing (Eq. (1)), and have spectral signatures similar to other albedo measurements (Brandt et al., 2005; Grenfell and Perovich, 2004; Gerland et al., 2004). However, the set-up affects the endmembers by giving more noisy (jagged) spectras with an unexpected dip at UV wavelengths and a jump at 1100 nm (corresponding to jumps in the transmission coefficient for the Lexan window) and substantial noise at high wavelength, so the endmembers curves were averaged with a running mean over every 30th wavelength to achieve smoother and more realistic curves (Fig. 5). The mean and standard deviations of the BRF were calculated for each sea-ice type by including only the spectra for those spectrometer foot-prints having a fraction larger than 90% of one sea-ice type (Tab. 5), *i.e.* not more than 10% of the pixels within the spectrometer foot-print may belong to other classes. For bare thick ice, no spectrometer footprint had a fraction of 90% or more, so the threshold limit was reduced to 75%, and therefore the error in the mean BRF for thick bare ice may be high (despite a low standard deviation in Tab. 5). Overall the BRF corresponds well with literature values for broadband albedo. The BRF for open water was slightly higher than corresponding albedo values from Brandt et al. (2005), because the open water was mixed with other types all having higher BRF. Allison et al. (1993) also experienced higher open water albedos than usual, due to snow covered ice in the vicinity of the open water scene (in that study a remote cosine collector was used, having 90% of its signal from a circle with radius approximately two times the hight of the instrument). The BRF of thin ice was 0.23 corresponding to values of young grey ice (Brandt et al., 2005), but with extremely large standard deviations evidently from tilt of the helicopter giving such high BRF as from snow covered ice and such low BRF as open water for the thin ice foot-prints. Previous measurements show that for bare ice, the reflectance factor takes a lower value than the albedo (Perovich, 1994). However, the thick ice BRF was higher than what is reported for snow-free first year ice albedo (Brandt et al., 2005), but this is due to mixing with snow covered ice, where on average 15% of the area within the foot-print was snow covered. The nadir reflectance factor and albedo should be similar at all wavelength for snow (Perovich, 1994), and this is in fact shown here where the snow covered sea ice have a BRF well inside the range of expected albedo values for dry snow (Paterson, 2001), and slightly higher than others (Brandt et al., 2005; Grenfell and Perovich, 1984).

	Snow covered ice	Thick bare ice	Thin ice	Open water
Mean(BRF)	0.86	0.63	0.23	0.09
σ(BRF)	0.22	0.16	0.36	0.16
♯ of samples	1058	7	7	99

Table 5
The mean and standard deviation (σ) of broadband reflectance factor (BRF). The bottom row gives the number of samples used for the calculations.

From the total set of ice thickness data obtained, we know that the thickness distribution at about 79° N exhibits a clear regional gradient from 10°W to 2°W, from thicker ice with a broad thickness distribution to thinner ice with a more narrow thickness distribution (Gerland et al., 2006). The modal ice thickness increases from east to west from about 2 m to almost 3 m (Fig. 12 lower panel). Most of the surface along the flight line is covered with sea ice, but leads occur regularly. Few ridges thicker than 6 m were observed. In general, the thickest ridges were found in the western part of the transect, with one ridge reaching a thickness of more than 10 m. However, airborne EM derived thicknesses can under-estimate thicknesses of ridges by the factor 2 or more (Pfaffling et al., 2006), indicating that real maxima ridge thickness might be at 20 m or more. Longer sections in the profile with no ice thicknesses near zero indicate large ice floes, in agreement with direct visual observations. The probability density functions (pdf) illustrate that the ice is different in the west and east of the investigation area (Fig. 11), which is consistent with the regional trend beyond the section selected for this paper (Gerland et al., 2006). At the marginal ice zone in the east, the modal ice thickness is 1.8 m (Fig. 11a), whereas in the west the distribution indicates thicker ice with the main mode at 2.6 m and an additional prominent mode at 1.1 m (Fig. 11b), indicating multi year and first year ice, respectively. The average sea-ice thickness (including snow) was 2.1 m with a standard deviation 1.3 m.
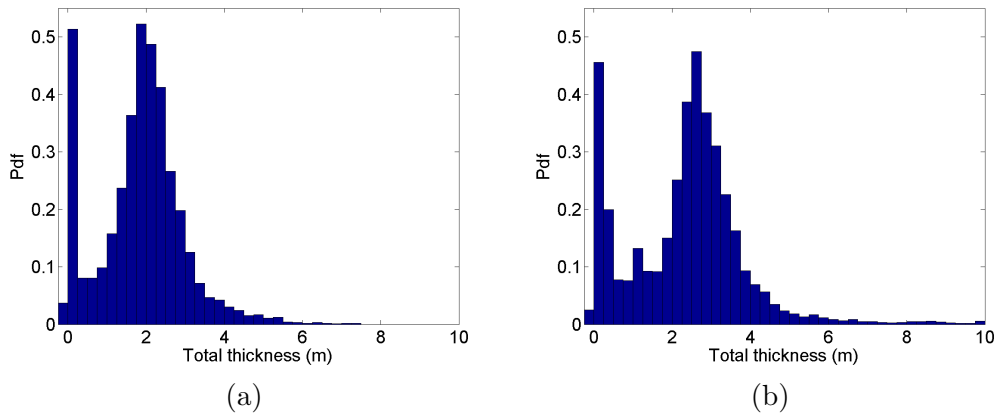

(a)   (b)

Fig. 11. Probability density function (pdf) of the total sea-ice thickness (sea ice plus snow) from the two transects 3-3.8° W in (a) and 3.8-4.6° W in (b) from the electromagnetic measurements.

The combination of the principal information from each instrument clearly shows that variations in measured BRF coincide well with changing sea-ice types (Fig. 12), where high BRF corresponds to large fractions of snow covered ice and low BRF corresponds to large fractions of open water. Small fractions of the two intermediate ice types, *e.g* at 3.7° west, lead to visible reduction in the BRF. The correlation coefficient between BRF and fractional coverage is 0.72 for snow covered ice (Fig. 13a) and -0.61 for open water (Fig. 13b), with large scatter of the samples. The BRF is not very dependent on the fractional coverage of thick ice (correlation coefficient is only -0.16), but slightly more on the thin ice (correlation coefficient of -0.30). The latter dependency is assumed to be higher if it were not for the tilt of the helicopter.
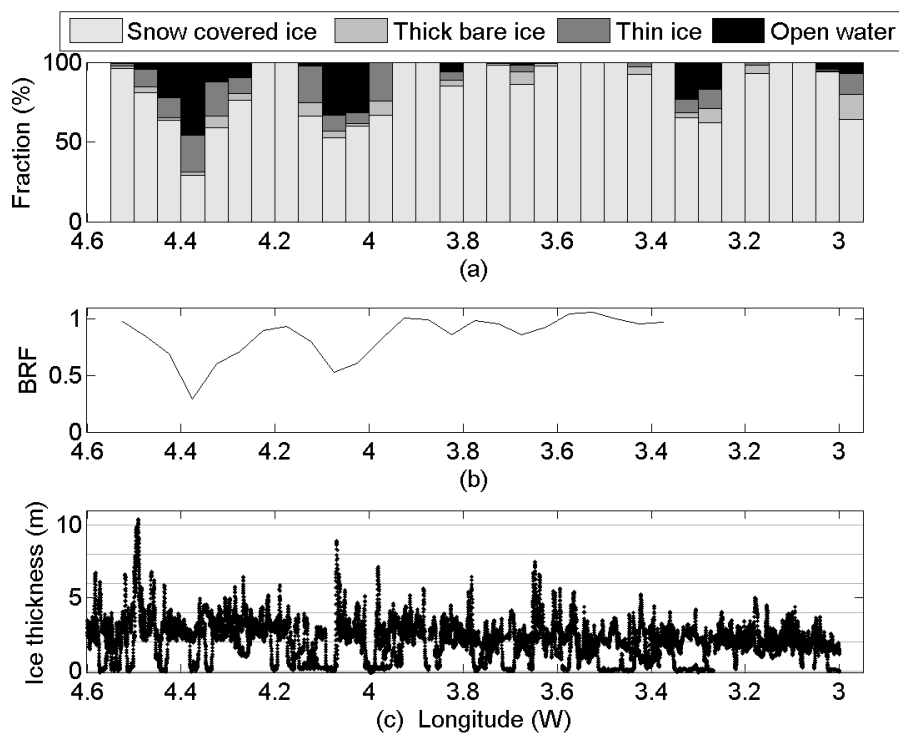

Fig. 12. (a) Average fractional coverage of the individual sea-ice types from the classified photographies and (b) average broadband reflectance factor (BRF) as a function of longitude for 0.05° longitude bands. (c) Average sea-ice thickness (ice plus snow) measured with the helicopter electromagnetic bird.

The correlation between sea-ice concentration and measured broadband albedo was 0.69. This was substantial higher than the correlations found by Laine (2004) using remote sensing data in the Arctic Ocean and Northern Hemisphere (0.34 and 0.56, respectively). The optical and EM measurements were taken from different transects, consequently with low correlation between sea-
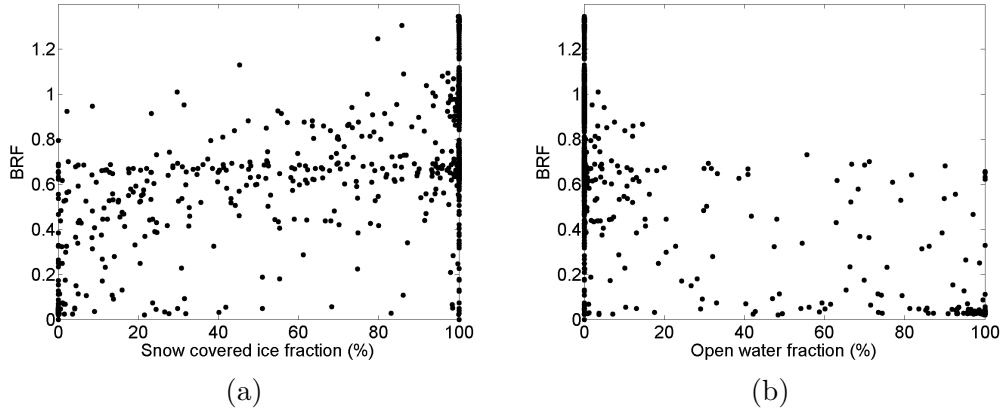
Fig. 13. Scatter-plot of broadband reflectance factor (BRF) and fractional snow covered ice in (a) and fractional open water in (b), with correlation coefficients of 0.72 and -0.61, respectively.

ice thickness and snow covered ice- or open water fractions (correlation coefficients of only 0.01 and -0.06, respectively). The average fraction of open water was 9.6%. In a recent study Perovich et al. (2007) emphasize the importance of a correct identification of open water areas due to the solar heating of the sea.

5   Conclusions

In this paper we have presented a method for finding the distribution of ice types along an airborne transect. This not only provides the major percentage of individual sea-ice types, sea-ice albedo and total sea-ice thickness in the over flown area, but it is a method which allows to compare (large amounts of) measurements in a consistent manner. The principal information from the three methods applied give the sea-ice types from digital photography, the spectral and broadband reflectance factor from the spectrometer and the total sea-ice thickness from the EM-bird measurements (Fig. 12). Together these three datasets completely describe the complex sea-ice environment: the sea-ice extent is described by combining the three ice types and separating it from open water, sea-ice volume is calculated as the sea-ice extent multiplied with the thickness, and the energy balance is determined from the optical measurements. As one important result, we can state that all three datasets are required, since for example the east-west ice thickness gradient does not appear in the image or optical observations. Since most of the sea ice is covered by relatively thick snow, and the albedo is completely determined by a snow cover of only a few cm thickness (Allison et al., 1993), snow covered multiyear ice and first year ice is difficult, if not impossible to distinguish without thickness measurements. However, if one dataset is missing (due to lack or failure

of instruments) the necessity information can, to some extent, be extracted from the other measurements, but with increased error (Figs. 7 and 9). The average root mean square errors for employing spectral unmixing for sea-ice classification are 0.034, 0.027, 0.021 and 0.028 for snow covered ice, thick bare ice, thin ice and open water, respectively, while for using the inverse spectral unmixing for calculating broadband reflectance factor (BRF) is 0.048. This is not evident for the EM measurements. Despite the fractional coverage of sea-ice types can be extracted from all three datasets individually, remember the neural network uses textural features for classifying the digital images, the spectral unmixing uses the optical features for classifying the reflectance measurements, and the thresholded EM data only consider the sea-ice thickness.

The average sea-ice fractions for the over flown area were 81.0% for snow covered ice, 4.0% for thick bare ice, 5.3% for thin ice and 9.6% for open water, thus the average sea-ice concentration was 90.3%. The average BRF was 0.73 with standard deviation 0.33, and the average sea-ice thickness (including snow) was 2.1 m with standard deviation 1.3 m. The average sea-ice volume is thus 2.1 times the area. Relative high correlations were found between the measured albedo and sea-ice concentration (0.69), however, the correlation would probably be higher if it were not for the tilt of the helicopter, and problems with the co-location of measurements.

This initial study sheds light on the enormous potential of integrated airborne surveys over sea ice with modern methods. Improvements of the individual set-ups and steps will reduce the temporal and spatial bias. This particularly concerns the optical measurements. Future solutions will also include optimizations of systems so that all methods can be operated on the same flight, optical sensors will be mounted outside the helicopter to avoid disturbing effects from windows, and the problem introduced by varying incoming solar radiation will be addressed by direct measurements of the incoming radiation, parallel to the nadir reflectance measurements. The co-location procedure will be improved, however, it is not straight forward to save large amounts of data instantaneously, and delays introduce offsets both in time and space between concurrent measurements. Also, the tilt of the helicopter offset the footprint of the image and spectrometer from the directly underlying field. In addition storage of raw images would be an important improvement allowing for standardization and correction of the images regarding shutter opening, exposure time and white balance. Some of these improvements are already under development and will be applied during campaigns as a part of projects in the International Polar Year (IPY) 2007-2009. With an improved set-up large amount of such measurements processed with the described methodology, providing sea-ice type fractions, albedo, thickness, extent and volume, will be extremely valuable datasets for *e.g.* validation of general circulation models and remote sensing products. Also, for applications with unmanned aerial vehicles (UAV) such an integrated airborne approach is required.

24

6 Acknowledgments

References

Allison, I., Brandt, R., and Warren, S. (1993). East Antarctic Sea Ice: Albedo, Thickness Distribution, and Snow Cover. *Journal of Geophysical Research*, 98:12417–12429.

Andersen, S., Breivik, L.-A., Eastwood, S., Godøy, Ø., Lind, M., Porcires, M. and Schyberg, H. (2005). *Sea Ice Product Manual*. Norwegian and Danish Meteorological Institutes.

Armstrong, T., Roberts, B., and Swithinbank, C. (1966). *Illustrated Glossary of Snow and Ice*. Special publication number 4. Scott Polar Research Institute, Cambridge.

Barber, D. G. and Le Drew, E. F. (1991). SAR Sea Ice Discrimination Using Texture Statistics: A Multivariate Approach. *Photogrammetric Engineering & Remote Sensing*, 57(4):385–395.

Bogdanov, A. V., Sandven, S., Johannessen, O. M., Alexandrov, V. Y., and Bobylev, L. P. (2005). Multisensor Approach to Automated Classification of Sea Ice Image Data. *IEEE Transactions on Geoscience and Remote Sensing*, 43(7):1648–1664.

Brandt, R. E., Warren, S. G., Worby, A. P., and Grenfell, T. C. (2005). Surface Albedo of the Antarctic Sea Ice Zone. *Journal of Climate*, 18:3606–3622.

Derksen, C., Piwowar, J. and LeDrew, E. (1997). Sea-Ice Melt-Pond Fraction as Determined from Low Level Aerial Photographs. *Arctic and Alpine Research*, 29(3),345–351.

Fetterer, F. and Untersteiner, N. (1998). Observations of Melt Ponds on Arctic Sea Ice. *Journal of Geophysical Research*, 103(C11):24821–24835.

Gerland, S., Haas, C., Hall, R., Holfort, J., Hansen, E., Løyning, T., and Renner, A. (2006). Spring Sea Ice Thickness in the Western Fram Strait: Preliminary Results. In Wadhams, P. and Amanatidis, G., editors, *Arctic Sea Ice Thickness: past, present & future. Proceedings of an international workshop at Rungstedgaard, Denmark, November 2005*, Climate Change and Natural Hazard Series 10. European Commission EUR 22416.

Gerland, S., Haas, C., Nicolaus, M., and Winther, J.-G. (2004). Seasonal Development of structure and Optical Properties of Fast Ice in Kongsfjorden, Svalbard. In Wiencke, C., editor, *The Coastal Ecosystems of Kongsfjorden, Svalbard*, number 492, pages 26–34. Alfred Wegner Institute for Polar & Marine Research.

Gonzalez, R. C. and Woods, R. E. (1992). *Digital Image Processing*. Addison-Wesley Publishing Company.

Grenfell, T. and Perovich, D. K. (2004). Seasonal and Spatial Evolution of Albedo in a Snow-Ice-Land-Ocean Environment. *Journal of Geophysical Research*, 109:1–15.

Grenfell, T. C. and Perovich, D. K. (1984). Spectral Albedos of Sea Ice and Incident Solar Irradiance in the Southern Beaufort Sea. *Journal of Geophysical Research*, 89(C3):3573–3580.

Haas, C., Gerland, S., Eicken, H., and Miller, H. (1997). Comparison of Sea-Ice Thickness Measurements Under Summer and Winter Conditions in the Arctic Using a Small Electromagnetic Induction Device. *Geophysics*, 62(3):749–757.

Haas, C., Goebell, S., Hendricks, S., Martin, T., Pfaffling, A., and von Saldern, C. (2006). Airborne Electromagnetic Measurements of Sea Ice Thickness: Methods and Applications. In Wadhams, P. and Amanatidis, G., editors, *Arctic Sea Ice Thickness: past, present & future. Proceedings of an international workshop at Rungstedgaard, Denmark, November 2005*, Climate Change and Natural Hazard Series 10. European Commission EUR 22416.

Haykin, S. (1999). *Neural Networks - A Comprehensive Foundation*. Prentice Hall.

Johnson, R. A. and Wichern, D. W. (2002). *Applied Multivariate Statistical Analysis*. Prentice Hall.

Kwok, R., Cunningham, G. F., and Pang, S. S. (2004). Fram Strait Sea Ice Outflow. *Journal of Geophysical Research*, 109(C01009).

Laine, V. (2004). Arctic Sea Ice Regional Albedo Variability and Trends, 1982-1998. *Journal of Geophysical Research*, 109(C06027).

Lythe, M., Hauser, A., and Wendler, G. (1999). Classification of Sea Ice Types in the Ross Sea, Antarctica from SAR and AVHRR Imagery. *International Journal of Remote Sensing*, 20(15 & 16):3073–3085.

Markus, T., Cavalieri, D. J., and Ivanoff, A. (2002). The Potential of Using Landsat 7 ETM+ for the Classification of Sea-Ice Surface Conditions during Summer. *Annals of Glaciology*, 34:415–419.

Massom, R. and Comiso, J. C. (1994). The Classification of Arctic Sea Ice Types and the Determination of Surface Temperature Using Advanced Very High Resolution Radiometer Data. *Journal of Geophysical Research*, 99(C3):5201–5218.

Nicodemus, F. E., Richmond, J. C., Ginsberg, I. W., and Limperis, T. (1977). Geometrical Considerations and Nomenclature for Reflectance. Technical report, U.S. Department of Commerce, National Bureau of Standards.

Paterson, W. S. B. (2001). *The Physics of Glaciers*. Butterworth Heinemann,

third edition.

Perovich, D. K. (1994). Light Reflection from Sea Ice During the Onset of Melt. *Journal of Geophysical Research*, 99(C2):3351–3359.

Perovich, D. K., Tucker, W. B. III and Ligett, K. A. (2002). Aerial Observations of the Evolution of Ice Surface Conditions during Summer. *Journal of Geophysical Research*, 107(C10):8048–8062.

Perovich, D. K., Light, B., Eicken, H., Jones, K. F., Runciman, K. and Nghiem, S. V. (2007). Increasing Solar Heating of the Arctic Ocean and Adjacent Seas, 1979-2005: Attribution and Role in the Ice-Albedo Feedback. *Geophysical Research Letter*, 34(L19505).

Pfaffling, A., Haas, C., and Reid, J. (2006). Key Characteristics of Helicopter Electromagnetic Sea Ice Thickness Mapping: Resolution, Accuracy and Footprint. In Wadhams, P. and Amanatidis, G., editors, *Arctic Sea Ice Thickness: past, present & future. Proceedings of an international workshop at Rungstedgaard, Denmark, November 2005*, Climate Change and Natural Hazard Series 10. European Commission EUR 22416.

Secretary of World Meteorological Organization (1970). WMO Sea-Ice Nomenclature. Technical report, World Meteorological Organization.

Steffen, K. (1986). Atlas of the Sea Ice types - Deformation Processes and Openings in the Cce. Technical report, ETH Geographisches Institut.

Theodoridis, S. and Koutroumbas, K. (1999). *Pattern Recognition*. Academic Press.

Tschudi, M. A., Curry, J. A., and Maslanik, J. A. (2001). Airborne Observations of Summertime Surface Features and Their Effect on Surface Albedo during FIRE/SHEBA. *Journal of Geophysical Research*, 106(D14):15335–15344.

Vikhamar, D. (2003). *Snow-Cover mapping in Forests by Optical Remote Sensing*. PhD thesis, Faculty of Mathematics and Natural Science, University of Oslo, Norway.

Vinje, T. (2001). Fram Strait Ice Fluxes and Atmospheric Circulation: 1950-2000. *Journal of Climate*, 14(16):3508–3517.